Layout optimization methodology of piezoelectric transducers in energy-recycling semi-active vibration control systems

Akihiro Takezawa[a,*], Kanjuro Makihara[b], Nozomu Kogiso[c], Mitsuru Kitamura[a]

[a] *Division of Mechanical Systems and Applied Mechanics, Institute of Engineering, Hiroshima University, 1-4-1 Kagamiyama, Higashi-Hiroshima, Hiroshima, Japan*
[b] *Department of Aerospace Engineering, Graduate School of Engineering, Tohoku University, 6-6-04 Aramaki Aza, Aoba, Aoba-ku, Sendai, Miyagi, Japan*
[c] *Department of Aerospace Engineering, Graduate School of Engineering, Osaka Prefecture University, 1-1 Gakuen-Cho, Naka-ku, Sakai, Osaka, Japan*

Abstract

An optimization methodology is proposed for the piezoelectric transducer (PZT) layout of an energy-recycling semi-active vibration control (ERSAVC) system for a space structure composed of trusses. Based on numerical optimization techniques, we intend to generate optimal location of PZTs under the constraint for the total length of PZTs. The design variables are set as the length of the PZT on each truss based on the concept of the ground structure approach. The transient problems of the mechanical and electrical vibrations based on the ERSAVC theory are considered as the equations of state. The objective is to minimize the integration of the square of all

*Corresponding author. Tel: +81-82-424-7544; Fax: +81-82-422-7194
Email addresses: akihiro@hiroshima-u.ac.jp (Akihiro Takezawa), makihara@ssl.mech.tohoku.ac.jp (Kanjuro Makihara), kogiso@aero.osakafu-u.ac.jp (Nozomu Kogiso), kitamura@hiroshima-u.ac.jp (Mitsuru Kitamura)

displacement over the whole analysis time domain. The sensitivity of the objective function is derived based on the adjoint variable method. Based on these formulations, an optimization algorithm is constructed using the fourth-order Runge-Kutta method and the method of moving asymptotes. Numerical examples are provided to illustrate the validity and utility of the proposed methodology. Using the proposed methodology, the optimal location of PZTs for the vibration suppression for multi-modal vibration is studied, which can be benchmark results of further study in the context of ERSAVC systems.
Keywords: , Optimal design, Semi-active vibration control, Sensitivity analysis, Piezoelectric actuator

1. INTRODUCTION

Vibration suppression is one of the most important issues in the design and operation of space structures. Due to limited launch capabilities, such structures need to be extremely light-weight although some structures succumb to vibrations because of their low structural stiffness. Moreover, vibrational energies are hard to disperse in the vacuum of space, in contrast to ground environments. These problems can be overcome by vibration control schemes. Much research has already been performed on the synthesis of the piezoelectric transducer (PZT) and electric devices, and the main structural vibration control methodologies [1, 2]. PZTs attached to or embedded in structures can convert mechanical energy into electrical energy and *vice versa*. These have been extensively used as actuators, sensors, and transducers for various purposes.

Vibration control schemes can be categorized into three types: active, passive and semi-active. In the active vibration control (AVC), a voltage or an electric charge has to be supplied from an external energy source to the PZTs. AVC systems basically provide the greatest vibration suppression among these three methodologies. However, for special structures that have limited energy sources, such as space structures and sea-based platforms, minimizing energy consumption is imperative. Moreover, since accurate models of large space structures are hard to construct due to difficulties with preliminary experiments and manufacturing errors of these structures, non-robust active vibration systems can potentially exhibit unstable behaviors.

The passive vibration control (PVC) in contrast is always stable, as no energy is supplied to the system. Compared with the AVC, these are easier to implement in actual systems, as no controllers, sensors, or filters are required. However, in most cases, vibration suppression is inferior compared with AVCs and, furthermore, performance levels might not be sufficient.

The third type, the semi-active vibration control (SAVC), dynamically changes some property of the structure according to feedback from the state, without adding extra energy. SAVC systems are usually able to achieve higher performance than PVC schemes without the disadvantages of AVC systems. Outlines of the various methods categorized as SAVC can be found in comprehensive reviews [3, 4, 5].

In this study, the focus of the work is on semi-active vibration suppression having energy-recycling capability with circuit switching [6, 7, 8, 9, 10]. For energy-recycling type SAVC schemes, controllers are composed of piezoelec-

tric materials and switchable circuits whose status is controlled according to the state of the controlled target. Richard *et al.* [6], Corr and Clark [7], and Onoda *et al.* [8] have proposed methods for the energy-recycling semi-active vibration control (ERSAVC) using an inductive circuit with a switching element. Depending on switching strategies, these energy-recycling systems are variously called SSDI, LR-switching, RL-shunt, and others. Such energy-recycling systems inherently possess energy-harvesting and energy-confinement mechanisms [9] that make vibration suppression effects much better than the ones of conventional semi-active systems. Their extended scheme, requiring an additional external voltage to provide further damping, so-called SSDV (synchronized switch damping on voltage), were also studied by Lefeuvre *et al.* [11], Badel *et al.* [12] and Ji *et al.* [13, 14]. Recently, Qiu *et al.* [10] presented an extensive overview of this field (*i.e.*, switching controls using piezoelectric materials for vibration suppression) that will enable readers to quickly grasp the history and significance of semi-active vibration suppression.

In ERSAVC systems, the improvement of the control logic and the circuit construction were mainly focused on [15, 16]. However, the location of PZTs, which is one of the most important design issues of the ERSAVC systems, especially for multi-modal vibration, has not been studied. In ERSAVCs, the vibration suppression is performed by varying the electric charge and voltage in a time scale of electrical circuit having shorter period than the structural one. This drastic change of control value nearly equals to applying impulse forces to the structure. Moreover, the timing of the control is based on the both structural and electrical time dependent state which is hard to be

predicted. This discontinuity and nonlinearity make us unable to introduce optimal location of PZTs in ERSAVCs theoretically. Thus, a numerical study is the only way to find the optimal location of PZTs in ERSAVCs.

Numerical optimization for the design of control systems, such as placement optimization of sensors and actuators, has long been studied for AVCs (*e.g.* [17, 18, 19, 20, 21]). The development of AVC optimization methodologies at early and middle stages is reviewed in [19, 22] respectively. The integrated optimization of the control system and the controlled structure has also been well-studied (*e.g.* [23, 24, 25, 26]). In AVCs, since the control theory which predicts the state of the system is well established, such as the theory of controllability and observability judged from the singular value of the Gramian, the outline of the optimal location of PZTs can be estimated without numerical optimization. However, to construct the system having the most effective vibration suppression with the lowest control energy, numerical optimization could be utilized. In this methodology, by integrating the numerical simulation of the system and gradient based optimization approach, the optimal solution could be found with a shorter time than the trial and error design.

Following the study for AVCs, we construct an optimization methodology for ERSAVC systems for a space structure composed of trusses proposed in [8] in this study. Based on approximation techniques and numerical optimization techniques, we intend to generate optimal location of PZTs under the constraint for the total length of PZTs within a reasonable analysis time. Moreover, using this methodology, the optimal location of PZTs for the vibration suppression for multi-modal vibration is studied, which can

be benchmark results of further study in the context of ERSAVC systems. First, the design variables chosen are the set of PZT lengths in the truss-elements. Physical properties of the PZT are expressed as functions of these design variables. Next, vibration analysis of the truss is formulated based on the transient response analysis using the modal method. The objective is to minimize the integral of the squares of all displacement over the whole analysis time domain. The sensitivity of the objective function is derived based on the adjoint variable method [27, 28]. Based on these formulations, an optimization algorithm is constructed using the method of moving asymptotes (MMA) [29]. Finally, we provide numerical examples for single and multi-mode vibration to illustrate the validity and usefulness of the proposed methodology and to obtain the mechanical aspect which could be useful for further design of ERSAVC systems from these results.

2. Numerical modeling of energy-recycling semi-active vibration control systems

2.1. Setup of the piezoelectric transducer

For modeling, a space frame truss, as sketched in Fig. 1, with some PZTs for vibration control is determined as the design target. First, the element comprising the PZT on the truss is defined. We consider a rod-type PZT, as depicted in Fig. 2, made of certain stacked piezoceramics. The piezoceramic plates are connected in electrically parallel. The PZT is connected to a truss and forms one rod element connecting two nodes of the structure. In the numerical analysis, the integrated structure is modeled to have only axial stiffness and piezoelectric behavior. Thus, the piezoelectric property of the

PZT can be expressed in terms of the truss element characteristics.

Figures 1 and 2 are about here.

Let l_p and δl_p be the length and elongation of the PZT respectively. The equations of state of the PZT comprising a stacked piezoceramic layer are formulated as follows [30]:

$$f_p = k_p \delta l_p - b_p Q \tag{1}$$

$$V = -b_p \delta l_p + \frac{Q}{C_p} \tag{2}$$

where f_p is the axial force applied to the PZT, and V and Q are its voltage and electric charge, respectively, with

$$k_p \equiv \frac{A_p \epsilon_{33}}{l_p(\epsilon_{33} s_{33} - {d_{33}}^2)} \tag{3}$$

$$b_p \equiv \frac{d_{33}}{n_p(\epsilon_{33} s_{33} - {d_{33}}^2)} \tag{4}$$

$$C_p \equiv \frac{A_p n_p^2(\epsilon_{33} s_{33} - {d_{33}}^2)}{l_p s_{33}} \tag{5}$$

where k_p, b_p, C_p and A_p are the axial stiffness, piezoelectric coefficient, capacitance and cross-sectional area of the PZT respectively; s, d and ϵ are compliance, piezoelectricity and permittivity of the PZT material, and n_p the number of the piezoceramic stacks.

We assume for simplicity that the PZT and the truss element have the same axial stiffness to avoid the change of eigenvalues and eigenvectors of the structure during the optimization. Let l and δl be the length and elongation

of the rod containing the PZT, the elongation of the PZT is expressed as follows:

$$\delta l_p = \frac{l_p}{l}\delta l \tag{6}$$

2.2. Equations of state for the truss with PZTs

The structure is composed of n_e linear truss elements having n_n node points and n_p PZTs. Let m be the number of degrees of freedom of this model. Considering as the state variables the displacement vector $\mathbf{u}$ at the nodes and the electric charge vector $\mathbf{Q}$ at the PZTs, the following equation of motion and piezoelectric equation are taken as the equations of state:

$$\mathbf{M\ddot{u}} + \mathbf{C\dot{u}} + \mathbf{Ku} = \mathbf{B_p Q} \tag{7}$$

$$\mathbf{V} = -\mathbf{B_p}^T\mathbf{u} + \mathbf{C_p}^{-1}\mathbf{Q} \tag{8}$$

where $\mathbf{M}$ is a mass matrix, $\mathbf{C}$ a damping matrix, $\mathbf{K}$ a stiffness matrix, $\mathbf{B_p}$ a piezoelectric coupling matrix, $\mathbf{V}$ an electric potential vector, and $\mathbf{C_p}$ a capacitance matrix.

For reasons of numerical effectiveness and to describe vibration suppression in terms of the modal coordinate system, the displacement $\mathbf{u}$ in global coordinates is transformed into a modal displacement $\mathbf{q}$ as follows:

$$\mathbf{u} = \boldsymbol{\phi}\mathbf{q} \tag{9}$$

where

$$\boldsymbol{\phi} \equiv [\phi_1, \phi_2, ..., \phi_m] \tag{10}$$

and ϕ_k is the k-th eigenvector of the following eigenvalue problem:

$$(\mathbf{K} - \omega_k^2\mathbf{M})\phi_k = 0 \tag{11}$$

where

$$\phi_k^T \mathbf{M} \phi_k = 1 \tag{12}$$

and ω_k is the k-th eigenfrequency. Substituting Eq. (9) into Eq. (7) and multiplying by $\boldsymbol{\phi}^T$ from the left, the following modal equation of state in terms of $\mathbf{q}$ is obtained.

$$\ddot{\mathbf{q}} + 2\boldsymbol{\Xi}\boldsymbol{\Omega}^{\frac{1}{2}}\dot{\mathbf{q}} + \boldsymbol{\Omega}\mathbf{q} = \boldsymbol{\phi}^T \mathbf{B_p} \mathbf{Q} \tag{13}$$

where

$$\boldsymbol{\Omega} \equiv \text{diagonal}[\omega_1^2, \omega_2^2, ..., \omega_m^2] \tag{14}$$

$$\boldsymbol{\Xi} \equiv \text{diagonal}[\xi_1, \xi_2, ..., \xi_m] \tag{15}$$

and ξ_k is the k-th modal damping ratio.

2.3. Energy-recycling semi-active vibration control

The control strategy of the ERSAVC used to effect vibration suppression within the structure [8] is outlined. In this modeling, an additional inductor and a switch are connected to each PZT which is modeled as a series connection of a voltage source, a capacitor and a resistor to form an LCR-circuit (see Fig. 3). With Q_i as state variable, the state equations for the i-th circuits containing the i-th PZT with the switch in the on or off position are represented as follows:

$$\text{When the i-th switch is on :} \qquad L_i\ddot{Q}_i + R_{pi}\dot{Q}_i + C_{pi}^{-1}Q_i = b_{pi}\delta l_{pi} \tag{16}$$

$$\text{When the i-th switch is off :} \qquad \dot{Q}_i = 0 \tag{17}$$

where L_i is the inductance of the circuit corresponding to the i-th PZT, and R_{pi}, C_{pi}, b_{pi} and δl_{pi} are the resistance, capacitance, piezoelectric coefficient and axial elongation of the i-th PZT. We assume that the PZT resistance is dominant in the circuit and the resistance of the inductor is enough small to be ignored.

Based partially on active control theory, the purpose of the switch is to initiate feedback control suppress vibration. The electric charge is stored in the PZT by changing the polarity of the charge. The control strategy of the ERSAVC is to actuate the switch of the circuit so that Q_i has the same sign as the target electric charge of the active control theory with an absolute value that is as large as possible. For the sake of simplicity, the target electric charge is set according to the direct feedback from the displacement velocity; that is, let Q_{Ti}, denote the target electric charge of the i-th PZT, then $Q_{Ti} = -\alpha\delta\dot{l}_{pi}$, where α is an arbitrary positive gain [31]. Assuming that the electric oscillation is much faster than the structural vibrations, the electric charge can be maintained at its maximum value if the switching occurs at half-periods in the electric oscillation. The operating law for the switch of the i-th PZT is formulated as follows:

$$\text{When } Q_{Ti}V_i < 0 \text{ turn on the switch for a duration of } \pi/\omega_{ci}, \tag{18}$$

where ω_{ci} is an eigenfrequency for the i-th circuit. After the switch is turned on, Q_i begins to decrease when V_i is positive, and vice versa. However, decreases (or increases) in Q_i do not continue for long because of electric oscillations. That is, this switching law means that the switch is turned on at the displacement peak for a half-period duration. Accordingly, electric charge keeps its peak value within a half period of the vibration until the next

displacement peak. Figure 4 shows the relationship between the displacement and the electric charge when the PZT is subjected to a sinusoidal forcing displacement. In short, electric charge is added only at the peak of the displacement, as shown in Fig. 4, to quickly transfer vibrational energy into electrical energy for damping.

Figures 3 and 4 are about here.

In the multi-degrees of freedom system, Q_{Ti} is determined from linear quadratic regulator (LQR) control theory. Taking electric charge $\mathbf{Q}$ of each PZT as control variables, the state equations in modal coordinate is rewritten:

$$\dot{\mathbf{z}} = \mathbf{A}\mathbf{z} + \mathbf{B}\mathbf{Q} \tag{19}$$

where

$$\mathbf{A} \equiv \begin{bmatrix} \mathbf{0} & \mathbf{I} \\ -\mathbf{\Omega} & -2\mathbf{\Xi}\mathbf{\Omega}^{\frac{1}{2}} \end{bmatrix} \tag{20}$$

$$\mathbf{z} \equiv \begin{bmatrix} \mathbf{q} \\ \dot{\mathbf{q}} \end{bmatrix} \tag{21}$$

$$\mathbf{B} \equiv \begin{bmatrix} \mathbf{0} \\ \boldsymbol{\phi}^T \mathbf{B_p} \end{bmatrix} \tag{22}$$

The optimal $\mathbf{Q}$ is obtained as the minimizer of the following cost function.

$$J = \int_0^\infty \left(\mathbf{z}^T \mathbf{W_1} \mathbf{z} + \mathbf{Q}^T \mathbf{W_2} \mathbf{Q} \right) \mathrm{d}t \tag{23}$$

where $\mathbf{W_1}$ and $\mathbf{W_2}$ are weighting matrices. Using the positive definite solution $\mathbf{P}$ of the following Riccati equation:

$$\mathbf{P}\mathbf{B_p}\mathbf{W_2}^{-1}\mathbf{P} - \mathbf{A}^T\mathbf{P} - \mathbf{P}\mathbf{A} - \mathbf{W}_1 = 0, \tag{24}$$

The matrix $\mathbf{Q_T}$ composed of Q_{Ti} is calculated as follows:

$$\mathbf{Q_T} \equiv -\mathbf{F}\mathbf{z} \tag{25}$$

where

$$\mathbf{Q_T} \equiv [Q_{T1}, Q_{T2}, ..., Q_{Tn_p}]^T \tag{26}$$

$$\mathbf{F} \equiv \mathbf{W_2}^{-1}\mathbf{B_p}^T\mathbf{P} \tag{27}$$

3. Optimization methodology

3.1. Design variables

In this study, we intend to obtain the optimal layout and length of the PZTs. Based on the ground structure approach [32] to truss optimization, candidates for the layout position are assigned to all truss elements comprising the target structure. That is, n_p equals n_e. The PZT lengths are considered as design variables for each truss, and in this regard very small design variables represent an absence of a PZT in the actual design based on the optimal result. The following length ratio vector between total bar length and the PZT $\mathbf{r}$ is also regarded as a design variable:

$$\mathbf{r} \equiv [r_1, r_2, ..., r_{n_p}] \tag{28}$$

where

$$r_i \equiv \frac{l_{pi}}{l_i} \tag{29}$$

$$r_{\min} \leq r_i \leq 1 \tag{30}$$

and $r_{\min}$ is the minimum value of r_i. The piezoelectricity b_{pi}, capacitance C_{pi} and resistance R_{pi} in Eqs. (13) and (16) depend on the length of the PZT. Assuming that the number of stacks n_{pi} of the i-th PZT is a linear continuous function of r_i as follows:

$$n_{pi} \approx n_{\max i} \times r_i \tag{31}$$

where $n_{\max i}$ is the number of stacks when $r_i = 1$. The coefficients of PZT in Eqs. (4) and (5) and the resister can be expressed as functions of r_i:

$$b_{pi} = \frac{b_0}{n_{pi}} \approx \frac{b_0}{n_{\max i}} r_i^{-1} \tag{32}$$

$$C_{pi} = \frac{A_{pi} n_{pi}^2 C_0}{l_{pi}} \approx \frac{A_{pi} n_{\max i}^2 C_0}{l_i} r_i \tag{33}$$

$$R_{pi} = \frac{R_0}{n_{pi}} = \frac{R_0}{n_{\max i}} r_i^{-1} \tag{34}$$

where

$$b_0 \equiv \frac{d_{33}}{\epsilon_{33} s_{33} - {d_{33}}^2} \tag{35}$$

$$C_0 \equiv \frac{\epsilon_{33} s_{33} - {d_{33}}^2}{s_{33}} \tag{36}$$

and R_0 is the resistance of a single layer of piezoceramic that forms the stack.

Note that, since the Riccati equation of Eq. (24) contains the piezoelectric matrix $\mathbf{B_p}$, the coefficient matrix $\mathbf{F}$ in Eq. (27) of the target electric charge

can vary during optimization. However, for simplicity, we would like to keep $\mathbf{F}$ constant during optimization. In the Riccatti equation Eq. (24), if $\mathbf{B_p}\mathbf{W_2}^{-1}$ is constant, the result becomes also constant independently of the value of $\mathbf{r}$. Thus, the weighting matrix $\mathbf{W_2}$ is set as a function of $\mathbf{r}$ to cancel out the effect of $\mathbf{r}$ in $\mathbf{B_p}$ as follows:

$$\mathbf{W_2} = w\text{diagonal}[\mathbf{r}] \tag{37}$$

where w is a positive coefficient.

3.2. The dependence of vibration suppression performance on the design variable

The relationship between the PZT length and vibration suppression is analyzed for a system with a single degree-of-freedom composed of truss and i-th PZT undergoing forced periodic displacement $u_0 \cos \omega t$. We assume the switching is performed at each maximum displacement. This is the ideal behavior for ERSAVC system, as shown in Fig. 4. In the steady state of the time harmonic forced vibration problem, the work done by the external force equals to the dissipation energy of the system. In the ERSAVC system, the energy dissipation occurs by converting the mechanical energy into the electrical energy by PZT. Thus, the work done by the PZT per cycle approximately equal to the energy transformation rate from mechanical to electrical energy, which is written [10]:

$$W_{\text{cycle}} = \frac{4b_{pi}C_{pi}\delta l_{pi}^2(1+\mathrm{e}^{-\zeta_{ci}\pi})}{(1-\mathrm{e}^{-\zeta_{ci}\pi})} \tag{38}$$

where

$$\zeta_{ci} \equiv \frac{R_{pi}}{2L_i\omega_{ci}} \tag{39}$$

$$\omega_{ci} \equiv \sqrt{\frac{1}{L_i C_{pi}}} \tag{40}$$

Substituting Eqs. (32)-(34) into Eq. (38), the energy transformation rate can be expressed as a function of the design variable r_i. W_{cycle} can also be used as the evaluation index of the energy dissipation of the system even in the transient problem. Using properties used in Section 5, the graph of W_{cycle} in the interval $0 < r_i \leq 1$ is presented as Fig. 5. A positive correlation is observed between PZT length and energy transformation rate; thus, a longer PZT achieves greater vibration suppression.

Figure 5 is about here.

3.3. Optimization problem

In the original paper of ERSAVC [8], time integral of the root mean square of displacements of all truss nodes is used as the evaluation criteria of the vibration suppression performance. Similarly, the time integration of the square norm of the displacement vector is used to define the objective function F of this optimization problem:

$$F(\mathbf{r}, \mathbf{u}, \mathbf{Q}) \equiv \int_0^T ||\mathbf{u}||^2 \mathrm{d}t \tag{41}$$

where T is the time when the evaluation ends. For the objective function having time integral form, the adjoint variable method [27, 28] can be applied

in its sensitivity analysis. As derived in the previous subsection, a positive correlation is observed between the PZT length and the vibration suppression effect. Thus, the optimal solution could have all possible PZTs at their maximum length. To reduce the maximum value of the total PZT length, a length constraint is introduced; the optimization problem is the represented as follows:

$$\underset{\mathbf{r}}{\text{minimize}}\, F(\mathbf{r}, \mathbf{u}, \mathbf{Q}) \tag{42}$$

subject to

$$\sum_{i=1}^{n_p} r_i l_p \leq l^U \tag{43}$$

$$r_{\min} \leq r_i \leq 1 \text{ for } i = 1, ..., n_p \tag{44}$$

and l^U is the upper bound for the total length of PZTs.

3.4. Sensitivity analysis

As the design variables are updated using MMA [29], we require the first-order sensitivity of the objective function and constraints to perform the optimization. Since the derivation is lengthy, only the results are shown here; a detailed derivation is shown in the Appendix. Using the adjoint variable method [27, 28], the derivative of the objective function with respect to the i-th design variable r_i defines a function of the state variable $\mathbf{Q}$ and the adjoint variables $\boldsymbol{\lambda}$ and $\boldsymbol{\mu}$:

$$\frac{dF}{dr_i} = -\int_0^T \boldsymbol{\lambda}^T \frac{\partial \mathbf{B_p}}{\partial r_i} \mathbf{Q} \mathrm{d}t + \int_{T_{Si}} \mu_i \left\{ \frac{\partial}{\partial r_i} \left(\frac{R_{pi}}{L_i} \right) \dot{Q}_i + \frac{\partial}{\partial r_i} \left(\frac{1}{R_{pi} L_i} \right) Q_i \right\} \mathrm{d}t \tag{45}$$

and T_{Si} is the time when the i-th switch is on. The adjoint variables are obtained by solving the following adjoint equations:

$$\ddot{\boldsymbol{\eta}} + 2\boldsymbol{\Xi}\boldsymbol{\Omega}^{\frac{1}{2}}\dot{\boldsymbol{\eta}} + \boldsymbol{\Omega}\boldsymbol{\eta} = \boldsymbol{\phi}^T(\mathbf{B_0}\boldsymbol{\mu} - 2\mathbf{u}) \tag{46}$$

$$\boldsymbol{\alpha}\ddot{\boldsymbol{\mu}} - \boldsymbol{\beta}\dot{\boldsymbol{\mu}} + \boldsymbol{\gamma}^T\boldsymbol{\mu} = -\mathbf{B_p}^T\boldsymbol{\lambda} \tag{47}$$

where

$$\boldsymbol{\alpha} \equiv \text{diagonal}\left[\alpha_1, \alpha_2, ..., \alpha_{n_p}\right],\ \alpha_i \equiv \begin{cases} \text{When } i\text{-th switch is on}: 1 \\ \text{When } i\text{-th switch is off}: 0 \end{cases} \tag{48}$$

$$\boldsymbol{\beta} \equiv \text{diagonal}\left[\beta_1, \beta_2, ..., \beta_{n_p}\right],\ \beta_i \equiv \begin{cases} \text{When } i\text{-th switch is on}: \frac{R_{pi}}{L_i} \\ \text{When } i\text{-th switch is off}: 1 \end{cases} \tag{49}$$

$$\boldsymbol{\gamma} \equiv \text{diagonal}\left[\gamma_1, \gamma_2, ..., \gamma_{n_p}\right],\ \gamma_i \equiv \begin{cases} \text{When } i\text{-th switch is on}: \frac{1}{L_i C_{pi}} \\ \text{When } i\text{-th switch is off}: 0 \end{cases} \tag{50}$$

$$\boldsymbol{\lambda} = \boldsymbol{\phi}\boldsymbol{\eta} \tag{51}$$

and $\mathbf{B_0}$ is a matrix to represent the diagonal matrix $\mathbf{D}$ as a linear form $\mathbf{B_0}^T\mathbf{u}$ as follows:

$$\mathbf{B_0}^T\mathbf{u} \equiv \mathbf{D} \tag{52}$$

where

$$\mathbf{D} \equiv \text{diagonal}\left[D_1, D_2, ..., D_{n_p}\right],\ D_i \equiv \begin{cases} \text{When } i\text{-th switch is on}: b_{pi}\delta l_{pi} \\ \text{When } i\text{-th switch is off}: 0 \end{cases} \tag{53}$$

The above adjoint equations are solved with the following terminal conditions:

$$\boldsymbol{\eta}(T) = \mathbf{0},\ \dot{\boldsymbol{\eta}}(T) = \mathbf{0},\ \boldsymbol{\mu}(T) = \mathbf{0},\ \dot{\boldsymbol{\mu}}(T) = \mathbf{0} \tag{54}$$

4. Numerical implementation

4.1. Algorithm

The optimization algorithm is shown in Fig. 6. The eigenvalues and eigenvectors of the system in Eq. (11) and the feed-back matrix of the LQR control theory in Eq. (27) are calculated first since these do not vary during optimization. In the optimization loop, the state equations and adjoint equations are solved by the fourth-order Runge-Kutta method. The state equations are an initial value problem, whereas the adjoint equations are a terminal value problem. The design variables are updated by MMA [29] using the calculated sensitivity.

Figure 6 is about here.

4.2. Approximation of state and adjoint equations

The approximation of the circuit equation in Eq. (16) and its corresponding adjoint equation in Eq. (47) is discussed with the purpose to reduce the computational cost. The eigenfrequencies of the vibration equation for the structure in Eq. (13) do not vary during optimization because mass and stiffness of the structure are fixed. The same thing can be said of the corresponding adjoint equations in Eq. (46). However, the eigenfrequency of Eqs. (16) and (47) can vary during optimization since the coefficient of the equation is a function of the design variable. According to Eq. (40), the eigenfrequency of the circuit with the lowest design variable $r_{\min}$ is $\sqrt{r_{\min}}^{-1}$ times the one with the highest design variable 1. In general, the step size of

the Runge-Kutta method must be chosen small enough compared with the period of the highest-order vibration to prevent divergence of the solution. Thus, the required time-step for the circuit equation can be $\sqrt{r_{\min}}$ times its maximum value when the design variable is at its minimum value. It could cause an increase in the computational cost even though the equation corresponds to a closed switch.

To avoid this problem, an approximation to Eq. (16) is used instead. Let us again consider the system with a single degree of freedom described above. Figure 7 shows a sketch of the time-variation of the electric charge around the time when the switch is closed. The electric charge increases or decreases according to Eq. (16) during a half-period of the electrical vibration. Assuming that the period of the electrical vibration is short enough compared with the period of the mechanical vibration and the PZT elongation does not vary during this switch ON period, the electric charge after that time Q_{after} can be calculated analytically as follows:

$$Q_{\text{after}} = -Q_{\text{before}}\mathrm{e}^{-\zeta_{ci}\pi} + b_{pi}\delta l_{pi}C_{pi}(1 + \mathrm{e}^{-\zeta_{ci}\pi}) \tag{55}$$

where Q_{before} is the electric charge at the time the switch is just closed. A detailed derivation is given in the Appendix. We vary the electric charge according to this equation at a quarter of the period after closing the switch instead of solving Eq. (16) directly. The approximated electric charge is also shown in Fig. 7. The adjoint equation in Eq.(47) is also solved by the same approximation.

Figure 7 is about here.

5. Numerical Examples

The following numerical examples are provided to confirm the validity and usefulness of the proposed methodology using the truss shown in Fig. 1. In all examples, the aluminum truss element has stiffness 1.99×10^6N/m and length density 9.5×10^{-2}kg/m. For simplicity, the PZT is assumed to have the same stiffness, density and cross-sectional area. Other PZT properties required in Eqs. (32)-(34) are set as follows: $b_0 = 1.31 \times 10^8$N/C, $A_p = 2.88 \times 10^{-5}$m^2, $C_0 = 2.28 \times 10^{-7}$F, $R_0 = 1.97 \times 10^3\Omega$, and $n_{\max} = 1300$. The length of each bay is set as 0.38m. Masses of 0.5kg are mounted at all nodes of the 4-th and 5-th bays. All the above physical factors are based on experimental data given in [9]. The minimum value $r_{\min}$ of the design variable is set to 10^{-3}.

All eigenmodes are used in performing calculations in the modal coordinate system. The first to the sixth-order eigenmodes and their corresponding eigenfrequencies are shown in Fig. 8. During the optimization, the PZTs are fixed to all truss elements. For simplicity, the maximum length of PZT is set to 0.38m which equals the length of the bay in all elements. The coefficient w in the weighting matrix $\mathbf{W_2}$ in Eq. (23) is set to 1.0×10^6. The time-step for the integration is set to 1.0×10^{-5}s, sufficiently shorter than the period of the highest-order vibration of the structure (4.88×10^{-4}s). The upper bound for the sum of the design variables of Eq. (43) is set to 13 which corresponds to 10% of the maximum total length of the PZTs.

Figure 8 is about here.

5.1. Confirming the validity of the approximation to the state and adjoint equations

The validity of the approximation to the equations of state, Eq. (16), and the adjoint equation, Eq. (47), using Eq. (55) is first confirmed. As the benchmark example, the first dominant mode of free vibration is considered. The initial modal velocity is set to $0.1\text{m} \cdot \text{kg}^{\frac{1}{2}}/\text{s}$ for the first mode and 0 for all other modes. The integration time for the state equations is set from 0 to 1s. All design variables are set to unity. Table 1 shows a comparison of the objective function in Eq. (41) between the direct calculation and the approximate calculation.

Table 1: Comparison between the objective functions calculated by direct and approximate methods

Calculation method	Direct	Approximate	Error
Objective function	2.42×10^{-7}	2.41×10^{-7}	0.57%

The validity of the analytical sensitivity derived from Eq. (45) was established by comparing the results with numerical sensitivities obtained using the finite difference method (FDM), performed according to following equation:

$$F'(r_i) = \frac{F(\mathbf{r} + \mathbf{a}_i \Delta c) - F(\mathbf{r})}{\Delta c}, \ (i = 1, ..., n) \tag{56}$$

where n is the number of design variables, $\mathbf{a}_i$ is a vector for which the i-th element is 1 and all other elements are 0, and Δc is set to 10^{-3}. In this example, the initial modal velocity is set to $0.1\text{m} \cdot \text{kg}^{\frac{1}{2}}/\text{s}$ for the first mode and 0 for all the other modes. The weighting matrix $\mathbf{W}_1$ in Eq. (23) is set to $\mathbf{W}_1 = \text{diagonal}[1, 1/\omega_1^2]$. The integration time for the state and adjoint

equations is set from 0 to the first eigen-period to maintain stable computation of the analytical sensitivity. The design variable $\mathbf{r}$ is set uniformly to 0.5. The objective function used in Eq. (56) is calculated by the direct method. The analytical sensitivity using the adjoint variable calculated by the approximate method is compared with the FDM sensitivity. Each result is normalized to unit norm. The least-squares error of the analytical sensitivity with respect to the corresponding FDM value was 0.15%. Figure 9 shows a bar-graph comparison of the top 14 sensitivities of both types. The numbers of elements corresponding to these sensitivities are shown in Fig. 10. This figure indicates elements with high sensitivities are located on the upper and lower parts of the structure. Since only small differences are observed in this figure, the analytical sensitivity can be regarded as having sufficient accuracy for optimization.

Figures 9 and 10 are about here.

5.2. Optimization for the first mode vibration

As the first benchmark example, optimization is performed of the PZT layout and length for the first dominant mode of free vibration. The initial value of design variable $\mathbf{r}$ is set uniformly to 0.1. The same integration time from 0 to the first eigen-period is introduced to perform a stable calculation of the sensitivity and low computational cost. When performing the analysis with the integration time 0 to five times the first eigen-period, the squared norm of the displacement integrated from 0 to the first eigen-period made

up 78.4% of the objective function in the initial layout. Thus, we consider the integration time up to the first eigen-period is sufficient for the performance evaluation during the optimization. Other analysis conditions are set the same as the previous sensitivity analysis example. Figure 11 shows the optimal r of each PZT after 100 iterations. The optimal length for each PZT is represented in the grayscale. The base trusses are plotted with dashed lines. Figure 12 shows the convergence history of the objective function. Long PZTs are located on the upper and lower sides of the structure with the length constraint becoming active. Figure 13 shows the top 14 design variables and maximum forces of these elements in the time history of the analysis of the optimal layout. The top 14 maximum forces were observed in the same elements with the top 14 design variables as a result. These were also identical to the elements with the top 14 sensitivities shown in Fig. 9. Since the design variables strongly correlated with the maximum forces, this layout is mechanically reasonable. Moreover, stable convergence is observed in Fig. 12 showing that in this example optimization has worked correctly. Figure 14 shows the variations in the PZT electric charge of the No.3 element shown in Fig. 10 and the first modal displacement of the optimal structure. ERSAVC performs electric charging only at the peak of the displacement, as shown in Fig. 4, to quickly transfer vibrational energy into electrical energy for damping. As switching is performed near the peak of the displacement and the PZT has been efficiently charged, ERSAVC has definitely worked well in this example. To confirm the performance improvement of the optimal layout over the initial, a re-analysis was performed with the longer integration time from 0 to five-times the first eigen-period. Figure 15 shows

the time histories of the squared norm of the total displacement and the norm of the total electric charge. In the optimal layout, quicker damping was observed together with quicker electric-charging of the PZTs. In this analysis, the objective function which is the time integral of the squared norm of the total displacement was reduced by about 16.2% from 2.95×10^{-7} to 2.48×10^{-7}.

Figures 11, 12, 13, 14 and 15 are about here.

5.3. Optimization for other vibrations and evaluation of optimal results

As the second example, optimizations for the following types of vibration are performed: the higher-order vibration of the vertical bending mode, the torsional vibration, the integrated vibration of the vertical and horizontal bending, and the integrated vibration of the vertical bending and torsion. Labeling the first dominant mode studied above as Case 1, these next studies are referred to as Case 2 through Case 5. The initial conditions for each of these vibrations are listed in Table 2. Cases 6 and 7 are used only to evaluate optimal configurations. All initial conditions and choices of weighting matrix $\mathbf{W}_1$ are listed in this table. The integration time for the state and adjoint equations is set from 0 to the first eigen-period in the same way as the first optimization example. The initial value of design variable $\mathbf{r}$ is set uniformly to 0.1.

Table 2: Initial conditions used in optimization and evaluation for certain free vibrations

Case No.	Description	Initial condition	$\mathbf{W}_1$ in Eq. (23)
1	First-order vertical bending	1st modal velocity is 0.1	diagonal$[1, 1/\omega_1^2]$
2	Second-order vertical bending	3rd modal velocity is 0.1	diagonal$[1, 1/\omega_3^2]$
3	First-order torsion	4th modal velocity is 0.1	diagonal$[1, 1/\omega_4^2]$
4	Integration of the first-order vertical and horizontal bending	1st and 2nd modal velocities are 0.1	diagonal$[1, 1, 1/\omega_1^2, 1/\omega_2^2]$
5	Integration of the first-order vertical bending and torsion	1st and 4th modal velocities are 0.1 and 0.2	diagonal$[1, 1, 1/\omega_1^2, 1/\omega_4^2]$
6	Vibration after vertical initial velocity	Velocity of the right bottom side is $[0\ 0\ 0.1]^T$	diagonal$[1, ..., 1, 1/\omega_1^2, ..., 1/\omega_6^2]$
7	Vibration after xyz-directional initial velocity	Velocity of the right bottom side is $[0.1\ 0.1\ 0.1]^T$	diagonal$[1, ..., 1, 1/\omega_1^2, ..., 1/\omega_6^2]$

Figure 16 shows optimal configurations for vibrations corresponding to Cases 2 through 5. The improvement of the objective functions in each optimization is shown in Table 3. In all optimizations, reductions in the objective functions were observed. Since the second-order bending vibration is dominant in Case 2, two separate segments of the long PZT can be observed in Fig. 16(a) on the both upper and lower sides. In Fig. 16(b), long PZTs are located on the diagonal members under torsional vibrations. Figure 16(c) shows long PZTs in members on top, on both sides, and on the bottom near the left side under the integrated vibration of the horizontal and vertical first-order bending. Figure 16(d) is an integrated structure from Fig. 11 and Fig. 16(c) corresponding to the integrated vibration of the first-order bending and torsion. In the ERSAVC, PZTs should basically be located on the truss element with high elongation to store the electric charge effectively. Thus, all these structures can be regarded as mechanically reasonable.

Figure 16 is about here.

Table 3: Improvement of the objective function in the optimization for various vibration types

	Optimization under				
	Case 1	Case 2	Case 3	Case 4	Case 5 ($\times 10^{-9}$)
Objective function					
Initial	230.23	2.74	3.37	444.39	242.72
Optimal	222.56	2.54	2.87	439.27	231.41
Reduction rate [%]	3.33	7.49	16.45	1.15	4.66

The validity of these optimal configurations is confirmed by re-analysis. In addition to vibration studies of Cases 1 to 5, Cases 6 and 7 listed in Table 2 are used in the evaluation. Vibrations in Cases 1 to 5 were excited by the initial modal velocities that are far from the natural phenomenon. Thus, vibrations corresponding to possible natural vibrations excited by motion of the whole system are introduced. Case 6 is a free vibration with z directional velocities at the right bottom side of the structure. Case 7 is a free vibration with xyz directional velocities at the same point. The weighting matrix $\mathbf{W}_1$ is set as for the vibration suppression of the six lowest modes. Each vibration is applied to the five optimal systems shown in Figs.11 and 16. To clarify the performance difference, the integration time for the state and adjoint equations is set from 0 to five times the first eigen-period, which is longer than that used in the optimizations. Table 4 lists the objective function for each result. Rows correspond to each vibration case used in the optimization, and columns correspond to the vibration case used for evaluation. For Cases 1 through 5, each optimal system optimized for the same vibration exhibits

the highest vibration suppression performance (diagonal items in Table 4). For Case 6, the optimal system for Case 1 seems to be useful as the vibration might be dominated by vertical bending. For Case 7, the optimal system for Case 4 exhibits the highest performance. It would seem that horizontal bending is only considered in Case 4.

Table 4: Evaluation of optimal results under several types of vibrations

	Objective function in the analysis under						
	Case 1	Case 2	Case 3	Case 4	Case 5	Case 6	Case 7 ($\times 10^{-9}$)
Optimal result obtained in							
Case 1	247.59	2.55	4.27	987.03	308.27	1.09	5.16
Case 2	319.82	2.54	3.86	925.70	375.93	1.25	3.13
Case 3	427.22	6.72	2.82	1077.14	463.44	1.46	8.38
Case 4	257.04	3.94	5.63	494.66	367.20	1.23	2.14
Case 5	250.53	3.58	3.05	1291.83	247.27	1.11	6.73

6. Conclusion

In this study, we developed an optimization method for ERSAVC systems suitable for space structures composed of trusses. Based on the concept of the ground structure approach for the truss layout optimization, the lengths of the PZT on each truss element were chosen as design variables. Physical properties of the PZT were expressed as functions of these variables. Vibration analysis of the truss was performed based on the transient response analysis using the modal method. The objective function was taken to be the integral of the square of all displacements over the whole analysis time

domain. The sensitivity of the objective function was derived based on the adjoint variable method. Combining these formulations, an optimization algorithm was constructed using the MMA. Numerical examples were provided to demonstrate the validity of our method.

For all low-order modes, optimization of the PZT layout and length was successful. Performance evaluations were performed on several types of vibrations. The integrated vibration caused by initial global displacements was only considered in this evaluation. Ideally, this type of vibration should also be considered in the optimization. However, as mainly studied in the eigenvalue optimization in structural optimization (*e.g.* [33, 34]), optimization for multiple modes is usually a challenging problem. The same thing can be said of the proposed methodology presented in this paper. Thus, the design strategy for semi-active systems should be one in which optimization is performed for a few fundamental modes of the target vibration.

Acknowledgments

This work was supported by JSPS KAKENHI Grant Numbers 25820422 and 25630436.

Appendix A. Derivation of sensitivity

A detailed derivation of the sensitivity given in Eq. (45) and the adjoint equations in Eqs. (46) and (47) is presented. Note that the effect of varying the design variables during switching is ignored for simplicity. The equations

of state in Eqs. (7), (16) and (17) are first expressed in matrix form:

$$\mathbf{M}\ddot{\mathbf{u}} + \mathbf{C}\dot{\mathbf{u}} + \mathbf{K}\mathbf{u} = \mathbf{B_p}\mathbf{Q} \tag{A.1}$$

$$\begin{aligned} \boldsymbol{\alpha}\ddot{\mathbf{Q}} + \boldsymbol{\beta}\dot{\mathbf{Q}} + \boldsymbol{\gamma}\mathbf{Q} &= \mathbf{D} \\ &= \mathbf{B_0}^T\mathbf{u} \end{aligned} \tag{A.2}$$

In Eq. (53), the elongation δl_{pi} of the i-th PZT, expressed as $\delta l_{pi} = r_i \delta l_i$, in the integrated element comprising a truss and a PZT, as shown in Fig. 2. As the piezoelectric factor b_{pi} is inversely proportional to the design variable r_i, $\mathbf{B_0}$ becomes a constant matrix independent of the design variables. Thus, in Eqs. (A.1) and (A.2) only matrices $\mathbf{B_p}$, $\boldsymbol{\beta}$ and $\boldsymbol{\gamma}$ depend on the design variable $\mathbf{r}$.

The general objective function for the sensitivity analysis is defined as a time integral of a function h.

$$F(\mathbf{u}, \dot{\mathbf{u}}, \ddot{\mathbf{u}}, \mathbf{Q}, \dot{\mathbf{Q}}, \ddot{\mathbf{Q}}, \mathbf{r}, t) \equiv \int_0^T h(\mathbf{u}, \dot{\mathbf{u}}, \ddot{\mathbf{u}}, \mathbf{Q}, \dot{\mathbf{Q}}, \ddot{\mathbf{Q}}, \mathbf{r}, t)\mathrm{d}t \tag{A.3}$$

Introducing the adjoint state vector $\boldsymbol{\lambda}$ and $\boldsymbol{\mu}$, the Lagrangian is:

$$L \equiv \int_0^T h\mathrm{d}t + \int_0^T \boldsymbol{\lambda}^T(\mathbf{M}\ddot{\mathbf{u}} + \mathbf{C}\dot{\mathbf{u}} + \mathbf{K}\mathbf{u} - \mathbf{B_p}\mathbf{Q})\mathrm{d}t + \int_0^T \boldsymbol{\mu}^T(\boldsymbol{\alpha}\ddot{\mathbf{Q}} + \boldsymbol{\beta}\dot{\mathbf{Q}} + \boldsymbol{\gamma}\mathbf{Q} - \mathbf{B_0}^T\mathbf{u})\mathrm{d}t \tag{A.4}$$

Using this, the derivative of the objective function can be expressed as:

$$\frac{\mathrm{d}F}{\mathrm{d}\mathbf{r}} = \frac{\partial L}{\partial \mathbf{r}} + \frac{\partial L}{\partial \mathbf{u}}\frac{\mathrm{d}\mathbf{u}}{\mathrm{d}\mathbf{r}} + \frac{\partial L}{\partial \dot{\mathbf{u}}}\frac{\mathrm{d}\dot{\mathbf{u}}}{\mathrm{d}\mathbf{r}} + \frac{\partial L}{\partial \ddot{\mathbf{u}}}\frac{\mathrm{d}\ddot{\mathbf{u}}}{\mathrm{d}\mathbf{r}} + \frac{\partial L}{\partial \mathbf{Q}}\frac{\mathrm{d}\mathbf{Q}}{\mathrm{d}\mathbf{r}} + \frac{\partial L}{\partial \dot{\mathbf{Q}}}\frac{\mathrm{d}\dot{\mathbf{Q}}}{\mathrm{d}\mathbf{r}} + \frac{\partial L}{\partial \ddot{\mathbf{Q}}}\frac{\mathrm{d}\ddot{\mathbf{Q}}}{\mathrm{d}\mathbf{r}} \tag{A.5}$$

Each term is calculated as follows:

$$\frac{\partial L}{\partial \mathbf{r}} = \int_0^T \frac{\partial h}{\partial \mathbf{r}} \mathrm{d}t - \int_0^T \boldsymbol{\lambda}^T \frac{\partial \mathbf{B_p}}{\partial \mathbf{r}} \mathbf{Q} \mathrm{d}t + \int_0^T \boldsymbol{\mu}^T \left(\frac{\partial \boldsymbol{\beta}}{\partial \mathbf{r}} \dot{\mathbf{Q}} + \frac{\partial \boldsymbol{\gamma}}{\partial \mathbf{r}} \mathbf{Q} \right) \mathrm{d}t \tag{A.6}$$

$$\frac{\partial L}{\partial \mathbf{u}} \frac{\mathrm{d}\mathbf{u}}{\mathrm{d}\mathbf{r}} = \int_0^T \frac{\partial h}{\partial \mathbf{u}} \frac{\mathrm{d}\mathbf{u}}{\mathrm{d}\mathbf{r}} \mathrm{d}t + \int_0^T \boldsymbol{\lambda}^T \mathbf{K} \frac{\mathrm{d}\mathbf{u}}{\mathrm{d}\mathbf{r}} \mathrm{d}t - \int_0^T \boldsymbol{\mu}^T {\mathbf{B_0}}^T \frac{\mathrm{d}\mathbf{u}}{\mathrm{d}\mathbf{r}} \mathrm{d}t \tag{A.7}$$

$$\frac{\partial L}{\partial \dot{\mathbf{u}}} \frac{\mathrm{d}\dot{\mathbf{u}}}{\mathrm{d}\mathbf{r}} = \int_0^T \frac{\partial h}{\partial \dot{\mathbf{u}}} \frac{\mathrm{d}\dot{\mathbf{u}}}{\mathrm{d}\mathbf{r}} \mathrm{d}t + \int_0^T \boldsymbol{\lambda}^T \mathbf{C} \frac{\mathrm{d}\dot{\mathbf{u}}}{\mathrm{d}\mathbf{r}} \mathrm{d}t \tag{A.8}$$

$$\frac{\partial L}{\partial \ddot{\mathbf{u}}} \frac{\mathrm{d}\ddot{\mathbf{u}}}{\mathrm{d}\mathbf{r}} = \int_0^T \frac{\partial h}{\partial \ddot{\mathbf{u}}} \frac{\mathrm{d}\ddot{\mathbf{u}}}{\mathrm{d}\mathbf{r}} \mathrm{d}t + \int_0^T \boldsymbol{\lambda}^T \mathbf{M} \frac{\mathrm{d}\ddot{\mathbf{u}}}{\mathrm{d}\mathbf{r}} \mathrm{d}t \tag{A.9}$$

$$\frac{\partial L}{\partial \mathbf{Q}} \frac{\mathrm{d}\mathbf{Q}}{\mathrm{d}\mathbf{r}} = \int_0^T \frac{\partial h}{\partial \mathbf{Q}} \frac{\mathrm{d}\mathbf{Q}}{\mathrm{d}\mathbf{r}} \mathrm{d}t - \int_0^T \boldsymbol{\lambda}^T \left(\mathbf{B_p} \frac{\mathrm{d}\mathbf{Q}}{\mathrm{d}\mathbf{r}} \right) \mathrm{d}t + \int_0^T \boldsymbol{\mu}^T \left(\boldsymbol{\gamma} \frac{\mathrm{d}\mathbf{Q}}{\mathrm{d}\mathbf{r}} \right) \mathrm{d}t \tag{A.10}$$

$$\frac{\partial L}{\partial \dot{\mathbf{Q}}} \frac{\mathrm{d}\dot{\mathbf{Q}}}{\mathrm{d}\mathbf{r}} = \int_0^T \frac{\partial h}{\partial \dot{\mathbf{Q}}} \frac{\mathrm{d}\dot{\mathbf{Q}}}{\mathrm{d}\mathbf{r}} \mathrm{d}t + \int_0^T \boldsymbol{\mu}^T \left(\boldsymbol{\beta} \frac{\mathrm{d}\dot{\mathbf{Q}}}{\mathrm{d}\mathbf{r}} \right) \mathrm{d}t \tag{A.11}$$

$$\frac{\partial L}{\partial \ddot{\mathbf{Q}}} \frac{\mathrm{d}\ddot{\mathbf{Q}}}{\mathrm{d}\mathbf{r}} = \int_0^T \frac{\partial h}{\partial \ddot{\mathbf{Q}}} \frac{\mathrm{d}\ddot{\mathbf{Q}}}{\mathrm{d}\mathbf{r}} \mathrm{d}t + \int_0^T \boldsymbol{\mu}^T \left(\boldsymbol{\alpha} \frac{\mathrm{d}\ddot{\mathbf{Q}}}{\mathrm{d}\mathbf{r}} \right) \mathrm{d}t \tag{A.12}$$

Substituting Eqs. (A.6)-(A.12) into Eq. (A.5),

$$\begin{aligned} \frac{dF}{d\mathbf{r}} =& \int_0^T \frac{\partial h}{\partial \mathbf{r}} \mathrm{d}t - \int_0^T \boldsymbol{\lambda}^T \frac{\partial \mathbf{B_p}}{\partial \mathbf{r}} \mathbf{Q} \mathrm{d}t + \int_0^T \boldsymbol{\mu}^T (\frac{\partial \boldsymbol{\beta}}{\partial \mathbf{r}} \dot{\mathbf{Q}} + \frac{\partial \boldsymbol{\gamma}}{\partial \mathbf{r}} \mathbf{Q}) \mathrm{d}t \\ &+ \int_0^T \left(\frac{\partial h}{\partial \mathbf{u}} + \boldsymbol{\lambda}^T \mathbf{K} - \boldsymbol{\mu}^T {\mathbf{B_0}}^T \right) \frac{\mathrm{d}\mathbf{u}}{\mathrm{d}\mathbf{r}} + \left(\frac{\partial h}{\partial \dot{\mathbf{u}}} + \boldsymbol{\lambda}^T \mathbf{C} \right) \frac{\mathrm{d}\dot{\mathbf{u}}}{\mathrm{d}\mathbf{r}} + \left(\frac{\partial h}{\partial \ddot{\mathbf{u}}} + \boldsymbol{\lambda}^T \mathbf{M} \right) \frac{\mathrm{d}\ddot{\mathbf{u}}}{\mathrm{d}\mathbf{r}} \mathrm{d}t \\ &+ \int_0^T \left(\frac{\partial h}{\partial \mathbf{Q}} - \boldsymbol{\lambda}^T \mathbf{B_p} + \boldsymbol{\mu}^T \boldsymbol{\gamma} \right) \frac{\mathrm{d}\mathbf{Q}}{\mathrm{d}\mathbf{r}} + \left(\frac{\partial h}{\partial \dot{\mathbf{Q}}} + \boldsymbol{\mu}^T \boldsymbol{\beta} \right) \frac{\mathrm{d}\dot{\mathbf{Q}}}{\mathrm{d}\mathbf{r}} + \left(\frac{\partial h}{\partial \ddot{\mathbf{Q}}} + \boldsymbol{\mu}^T \boldsymbol{\alpha} \right) \frac{\mathrm{d}\ddot{\mathbf{Q}}}{\mathrm{d}\mathbf{r}} \mathrm{d}t \end{aligned} \tag{A.13}$$

If the equations in the second and third lines of Eq. (A.13) are zero, the

following adjoint equations are obtained by applying the integration by parts,

$$\mathbf{M}\ddot{\boldsymbol{\lambda}} + \mathbf{C}\dot{\boldsymbol{\lambda}} + \mathbf{K}\boldsymbol{\lambda} - \mathbf{B_0}\boldsymbol{\mu} = \left(-\frac{\partial h}{\partial \mathbf{u}} + \frac{\mathrm{d}}{\mathrm{d}t}\frac{\partial h}{\partial \dot{\mathbf{u}}} - \frac{\mathrm{d}^2}{\mathrm{d}t^2}\frac{\partial h}{\partial \ddot{\mathbf{u}}}\right)^T \tag{A.14}$$

$$\boldsymbol{\lambda}^T(T)\mathbf{M} + \frac{\partial h}{\partial \ddot{\mathbf{u}}}(T) = \mathbf{0} \tag{A.15}$$

$$\frac{\partial h}{\partial \dot{\mathbf{u}}}(T) + \boldsymbol{\lambda}^T(T)\mathbf{C} - \dot{\boldsymbol{\lambda}}^T(T)\mathbf{M} - \frac{\mathrm{d}}{\mathrm{d}t}\frac{\partial h}{\partial \ddot{\mathbf{u}}}(T) = \mathbf{0} \tag{A.16}$$

$$\boldsymbol{\alpha}\ddot{\boldsymbol{\mu}} - \boldsymbol{\beta}\dot{\boldsymbol{\mu}} + \boldsymbol{\gamma}^T\boldsymbol{\mu} - \mathbf{B_p}^T\boldsymbol{\lambda} = \left(-\frac{\partial h}{\partial \mathbf{Q}} + \frac{\mathrm{d}}{\mathrm{d}t}\frac{\partial h}{\partial \dot{\mathbf{Q}}} - \frac{\mathrm{d}^2}{\mathrm{d}t^2}\frac{\partial h}{\partial \ddot{\mathbf{Q}}}\right)^T \tag{A.17}$$

$$\boldsymbol{\mu}^T(T)\alpha + \frac{\partial h}{\partial \ddot{\mathbf{Q}}}(T) = \mathbf{0} \tag{A.18}$$

$$\frac{\partial h}{\partial \dot{\mathbf{Q}}}(T) + \boldsymbol{\mu}^T(T)\boldsymbol{\beta} - \dot{\boldsymbol{\mu}}^T(T) - \frac{\mathrm{d}}{\mathrm{d}t}\frac{\partial h}{\partial \ddot{\mathbf{Q}}}(T) = \mathbf{0} \tag{A.19}$$

If the objective function is the time integral of the square norm of the displacement vector in Eq. (41), the derivatives of function h can be obtained as follows:

$$\frac{\partial h}{\partial \mathbf{r}} = \mathbf{0},\ \frac{\partial h}{\partial \mathbf{u}} = 2\mathbf{u}^T,\ \frac{\partial h}{\partial \dot{\mathbf{u}}} = \mathbf{0},\ \frac{\partial h}{\partial \ddot{\mathbf{u}}} = \mathbf{0} \tag{A.20}$$

Substituting Eq. (A.20) into Eqs. (A.13)-(A.19), the sensitivity of the objective function is found to be:

$$\frac{dL}{d\mathbf{r}} = -\int_0^T \boldsymbol{\lambda}^T\frac{\partial \mathbf{B_p}}{\partial \mathbf{r}}\mathbf{Q}\mathrm{d}t + \int_0^T \boldsymbol{\mu}^T\left(\frac{\partial \boldsymbol{\beta}}{\partial \mathbf{r}}\dot{\mathbf{Q}} + \frac{\partial \boldsymbol{\gamma}}{\partial \mathbf{r}}\mathbf{Q}\right)\mathrm{d}t \tag{A.21}$$

Substituting Eq. (A.20) into Eq. (A.14), the adjoint equations become:

$$\mathbf{M}\ddot{\boldsymbol{\lambda}} + \mathbf{C}\dot{\boldsymbol{\lambda}} + \mathbf{K}\boldsymbol{\lambda} = \mathbf{B_0}\boldsymbol{\mu} - 2\mathbf{u} \tag{A.22}$$

$$\boldsymbol{\alpha}\ddot{\boldsymbol{\mu}} - \boldsymbol{\beta}\dot{\boldsymbol{\mu}} + \boldsymbol{\gamma}^T\boldsymbol{\mu} = -\mathbf{B_p}^T\boldsymbol{\lambda} \tag{A.23}$$

$$\boldsymbol{\lambda}(T) = \mathbf{0},\ \dot{\boldsymbol{\lambda}}(T) = \mathbf{0},\ \boldsymbol{\mu}(T) = \mathbf{0}, \dot{\boldsymbol{\mu}}(T) = \mathbf{0} \tag{A.24}$$

Moreover, the adjoint variable $\boldsymbol{\lambda}$ is transformed into its modal variable $\boldsymbol{\eta}$ using following equation.

$$\boldsymbol{\lambda} = \boldsymbol{\phi}\boldsymbol{\eta} \tag{A.25}$$

Substituting Eq. (A.25) into Eq. (A.22) and multiplying $\boldsymbol{\phi}^T$ from the left, the following equations are obtained:

$$\ddot{\boldsymbol{\eta}} + 2\boldsymbol{\Xi}\boldsymbol{\Omega}^{\frac{1}{2}}\dot{\boldsymbol{\eta}} + \boldsymbol{\Omega}\boldsymbol{\eta} = \boldsymbol{\phi}^T(\mathbf{B_0}\boldsymbol{\mu} - 2\mathbf{u}) \tag{A.26}$$

$$\boldsymbol{\eta}(T) = \mathbf{0},\ \dot{\boldsymbol{\eta}}(T) = \mathbf{0} \tag{A.27}$$

Note that since matrices $\boldsymbol{\alpha}$, $\boldsymbol{\beta}$ and $\boldsymbol{\gamma}$ are diagonal, Eq. (A.23) is decomposed into a set of ordinary differential equation by considering the state of each switch independently.

Appendix B. Derivation of approximated electric charge

Let us consider a system with a single degree of freedom composed of a truss with i-th PZT being subjected to a forced periodic displacement. Let us assume that the switch of the circuit is turned on when $t = 0$. The following equation is the state equation of this system:

$$\ddot{Q}_i + 2\zeta_{ci}\omega_{ci}\dot{Q}_i + \omega_{ci}^2 Q_i = \frac{b_{pi}}{L_i}\delta l_{pi} \tag{B.1}$$

where δl_{pi} is the elongation of PZT. The initial values of electric charge and PZT elongation are denoted Q_0 and u_0 respectively. Assuming that this elongation, because it is sufficiently shorter than the amplitude of the mechanical vibration, does not vary during the time when the switch is closed, the solution of this equation can be deduced as follows:

$$\begin{aligned} Q(t) =& (Q_0 - b_{pi}C_{pi}\delta l_{pi})[\cos\{\omega_{ci}\sqrt{1-\zeta_{ci}}t\} \\ &+ \frac{\zeta_{ci}}{\sqrt{1-\zeta_{ci}}}\sin\{\omega_{ci}\sqrt{1-\zeta_{ci}}t\}]\mathrm{e}^{-\zeta_{ci}\omega_{ci}t} + b_{pi}C_{pi}\delta l_{pi} \end{aligned} \tag{B.2}$$

Assuming that $\zeta_c \ll 1$, we simplify Eq. (B.2) as

$$Q(t) \approx (Q_0 - b_{pi}C_{pi}\delta l_{pi})\cos(\omega_{ci}t)\mathrm{e}^{-\zeta_{ci}\omega_{ci}t} + b_{pi}C_{pi}\delta l_{pi} \tag{B.3}$$

At $t = \pi/\omega_{ci}$, electric charge is

$$Q(\pi/\omega_{ci}) \approx -(Q_0 - b_{pi}C_{pi}\delta l_{pi})\mathrm{e}^{-\zeta_{ci}\pi} + b_{pi}C_{pi}\delta l_{pi} \tag{B.4}$$

Replacing $Q(\pi/\omega_{ci})$ and Q_0 by Q_{after} and Q_{before} respectively, Eq. (55) is obtained.

[1] G. A. Lesieutre. Vibration damping and control using shunted piezoelectric materials. Shock and Vibration Digest, 30(3):187–195, 1998.

[2] M. Ahmadian and A. P. Deguilio. Recent advances in the use of piezoceramics for vibration suppression. Shock and Vibration Digest, 33(1):15–22, 2001.

[3] D. Karnopp. Active and semi-active vibration isolation. Journal of Mechanical Design, 117:177–185, 1995.

[4] M. D. Symans and M. C. Constantinou. Semi-active control systems for seismic protection of structures: a state-of-the-art review. Engineering Structures, 21(6):469–487, 1999.

[5] N. Jalili. A comparative study and analysis of semi-active vibration-control systems. Journal of Vibration and Acoustics, 124(4):593–605, 2002.

[6] C. Richard, D. Guyomar, D. Audigier, and H. Bassaler. Enhanced semi-passive damping using continuous switching of a piezoelectric device on an inductor. Proceedings of SPIE, 3989:288–299, 2000.

[7] L. R. Corr and W. W. Clark. A novel semi-active multi-modal vibration control law for a piezoceramic actuator. Journal of Vibration and Acoustics, 125:214–222, 2003.

[8] J. Onoda, K. Makihara, and K. Minesugi. Energy-recycling semi-active method for vibration suppression with piezoelectric transducers. AIAA Jounal, 41(4):711–719, 2003.

[9] K. Makihara, J. Onoda, and K. Minesugi. Comprehensive assessment of semi-active vibration suppression including energy analysis. Journal of Vibration and Acoustics, 129:84–93, 2007.

[10] J. Qiu, H. Ji, and K. Zhu. Semi-active vibration control using piezoelectric actuators in smart structures. Frontiers of Mechanical Engineering in China, 4(3):242–251, 2009.

[11] E. Lefeuvre, A. Badel, L. Petit, C. Richard, and D. Guyomar. Semi-passive piezoelectric structural damping by synchronized switching on voltage sources. Journal of Intelligent Material Systems and Structures, 17(8-9):653–660, 2006.

[12] A. Badel, G. Sebald, D. Guyomar, M. Lallart, E. Lefeuvre, C. Richard, and J. Qiu. Piezoelectric vibration control by synchronized switching on adaptive voltage sources: Towards wideband semi-active damping. Journal of the Acoustical Society of America, 119:2815–2825, 2006.

[13] H. Ji, J. Qiu, A. Badel, and K. Zhu. Semi-active vibration control of a composite beam using an adaptive ssdv approach. Journal of Intelligent Material Systems and Structures, 20(4):401–412, 2009.

[14] H. Ji, J. Qiu, A. Badel, Y. Chen, and K. Zhu. Semi-active vibration control of a composite beam by adaptive synchronized switching on voltage sources based on lms algorithm. Journal of Intelligent Material Systems and Structures, 20(8):939–947, 2009.

[15] K. Makihara, J. Onoda, and K. Minesugi. Low-energy-consumption hybrid vibration suppression based on an energy-recycling approach. AIAA Journal, 43(8):1706–1715, 2005.

[16] K. Makihara, J. Onoda, and K. Minesugi. Novel approach to self-sensing actuation for semi-active vibration suppression. AIAA Journal, 44(7):1445–1453, 2006.

[17] G. Schulz and G. Heimbold. Dislocated actuator/sensor positioning and feedback design for flexible structures. Journal of Guidance, Control, and Dynamics, 6:361–367, 1983.

[18] R. E. Lindberg. On the number and placement of actuators for independent modal space control (for large flexible spacecraft). Journal of Guidance, Control, and Dynamics, 7:215–221, 1984.

[19] A. Hac and L. Liu. Sensor and actuator location in motion control of flexible structures. Journal of Sound and Vibration, 167(2):239–61, 1993.

[20] F. Gao, Y. Shen, and L. Li. The optimal design of piezoelectric actuators for plate vibroacoustic control using genetic algorithms with immune diversity. Smart Materials and Structures, 9:485, 2000.

[21] D. E. Heverly, K. W. Wang, and E. C. Smith. An optimal actuator placement methodology for active control of helicopter airframe vibrations. Journal of the American Helicopter Society, 46(4):251–261, 2001.

[22] M. I. Frecker. Recent advances in optimization of smart structures and actuators. Journal of Intelligent Material Systems and Structures, 14(4-5):207–216, 2003.

[23] A. L. Hale, W. E. Dahl, and R. J. Lisowiki. Optimal simultaneous structural and control design of maneuvering flexible spacecraft. Journal of Guidance, Control, and Dynamics, 8:86–93, 1985.

[24] J. Onoda and R. T. Haftka. An approach to structure/control simultaneous optimization for large flexible spacecraft. AIAA Journal, 25(8):1133–1138, 1987.

[25] I. Kajiwara, K. Tsujioka, and A. Nagamatsu. Approach for simultaneous optimization of a structure and control system. AIAA Journal, 32(4):866–873, 1994.

[26] J. S. Ou and N. Kikuchi. Integrated optimal structural and vibration control design. Structural Optimization, 12(4):209–216, 1996.

[27] E. J. Haug, K. K. Choi, and V. Komkov. Design Sensitivity Analysis of Structural Systems. Academic Press, Orlando, 1986.

[28] B. S. Kang, G. J. Park, and J. S. Arora. A review of optimization of structures subjected to transient loads. Structural and Multidisciplinary Optimization, 31(2):81–95, 2006.

[29] K. Svanberg. The method of moving asymptotes- a new method for structural optimization. International Journal for Numerical Methods in Engineering, 24(2):359–373, 1987.

[30] M. Nelkon. Electricity and Magnetism. Edward Arnold, second edition, 1965.

[31] M. J. Balas. Direct velocity feedback control of large space structures. Journal of Guidance, Control, and Dynamics, 2(3):252–253, 1979.

[32] M. P. Bendsøe and O. Sigmund. Topology Optimization: Theory, Methods, and Applications. Springer-Verlag, Berlin, 2003.

[33] Z. D. Ma, N. Kikuchi, and H. C. Cheng. Topological design for vibrating structures. Computer Methods in Applied Mechanics and Engineering, 121(1-4):259–280, 1995.

[34] A. Takezawa, S. Nishiwaki, and M. Kitamura. Shape and topology optimization based on the phasefield method and sensitivity analysis. Journal of Computational Physics, 229(7):2697–2718, 2010.

List of all figures

15. Time history of the squared norm of the total displacement and the norm of the total electric charge for the initial and optimal layouts of the PZT in a re-analysis.
16. Optimal layout of PZTs for various vibration types. (a) through (d) correspond to Cases 2 through 5 described in the text.

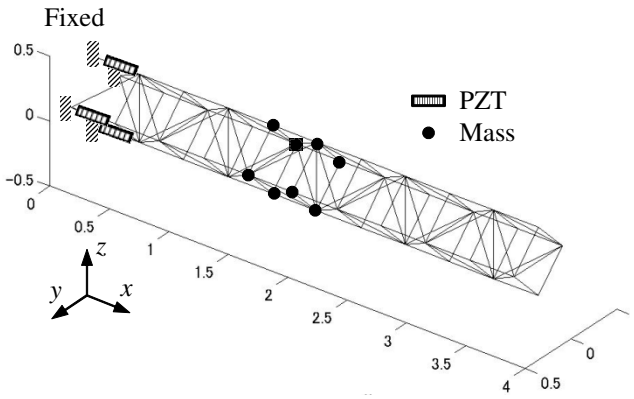

Figure 1: Vibration suppression target structure.

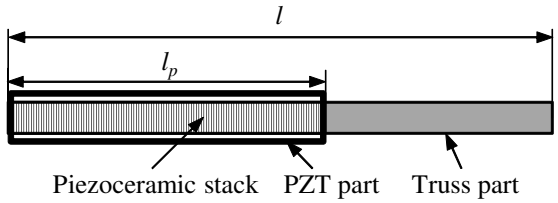

Figure 2: Outline of PZT connected with a truss.

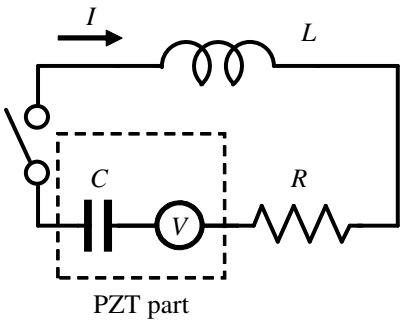

Figure 3: Equivalent LCR circuit of each PZT.

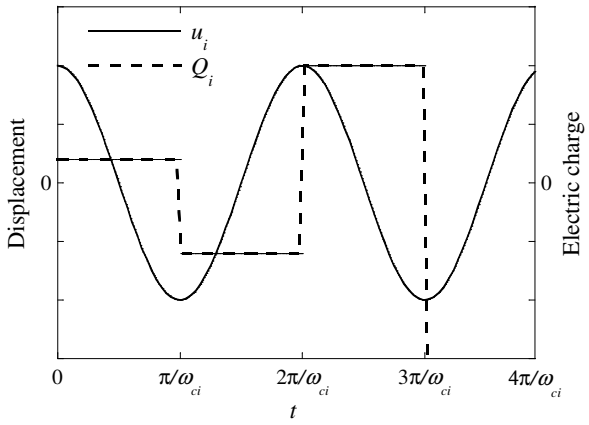

Figure 4: Outline of time-variation for displacement and electric charge under ERSAVC.

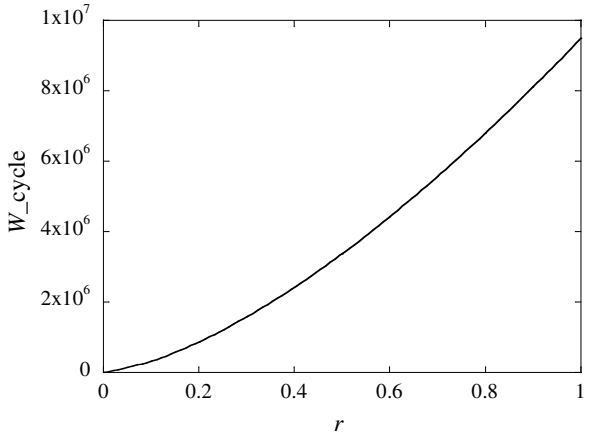

Figure 5: Dependence of energy transformation rate on design variables in the single DOF model.

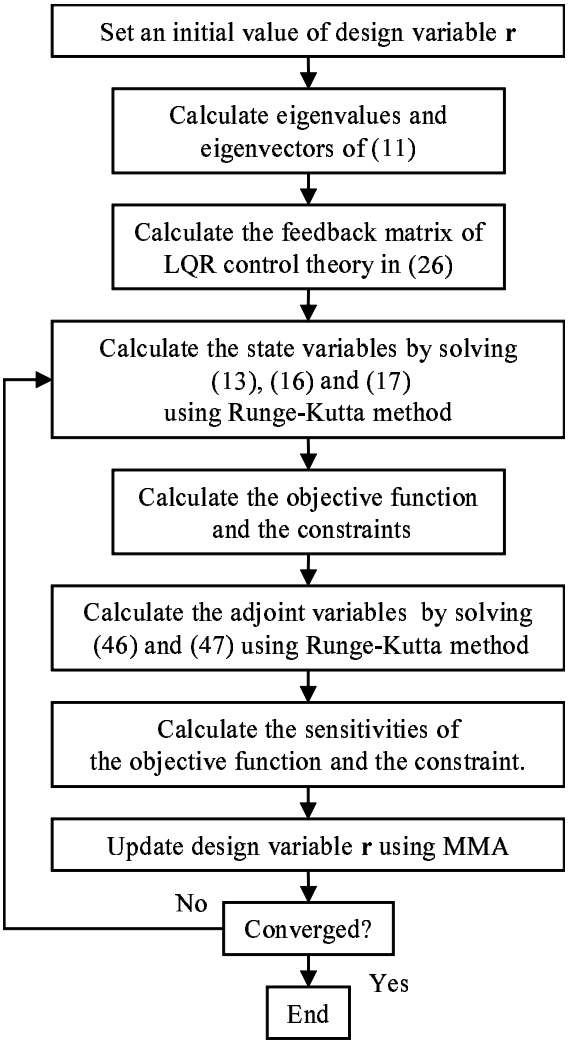

Figure 6: Flowchart of the optimization procedure.

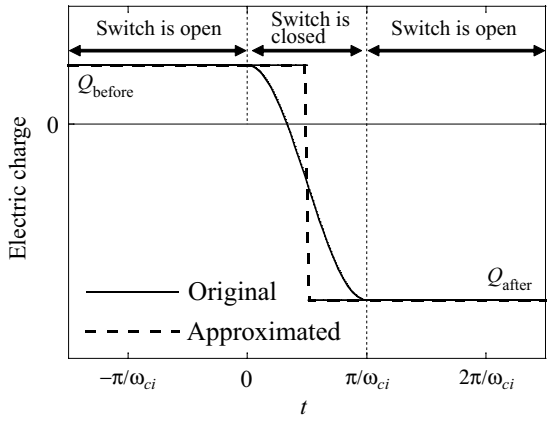

Figure 7: Approximation of the electric charge variation.

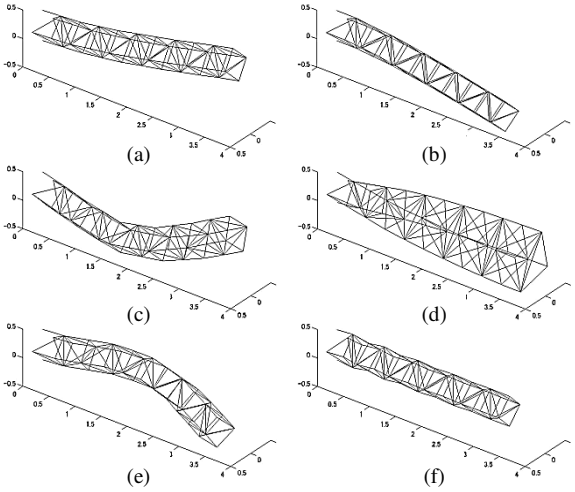

Figure 8: Eigenmode shapes: (a) The first mode (13.01Hz): vertical bending, (b) The second mode (13.40Hz): horizontal bending, (c) The third mode (53.32Hz): vertical bending, (d) The fourth mode (57.04Hz): torsion, (e) The fifth mode (57.83Hz): horizontal bending, (f) The sixth mode (128.48Hz): stretching.

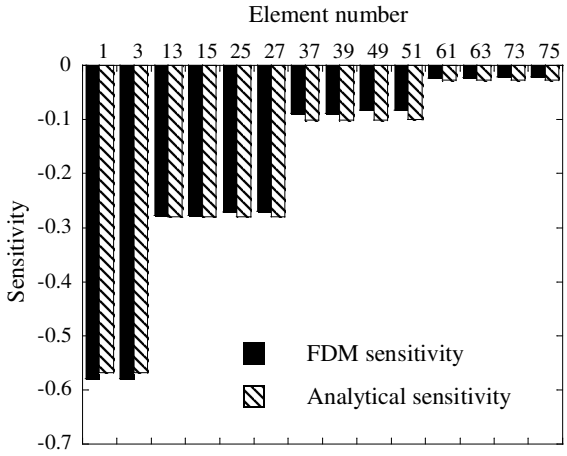

Figure 9: Comparison of the analytical sensitivity with the FDM sensitivity on the top 14 sensitivities.

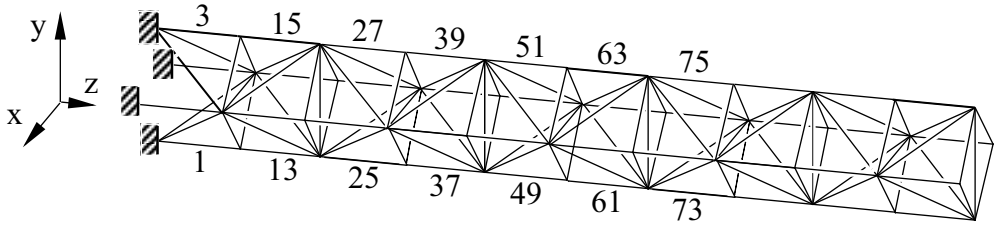

Figure 10: Element numbers corresponding to the top 14 sensitivities.

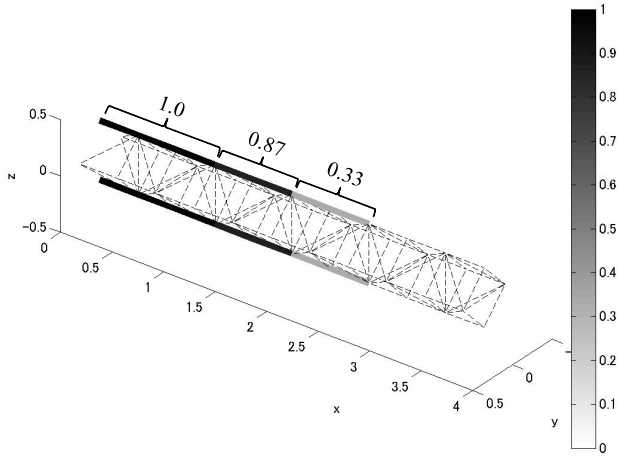

Figure 11: Optimal layout of PZT for the first dominant mode of free vibration.

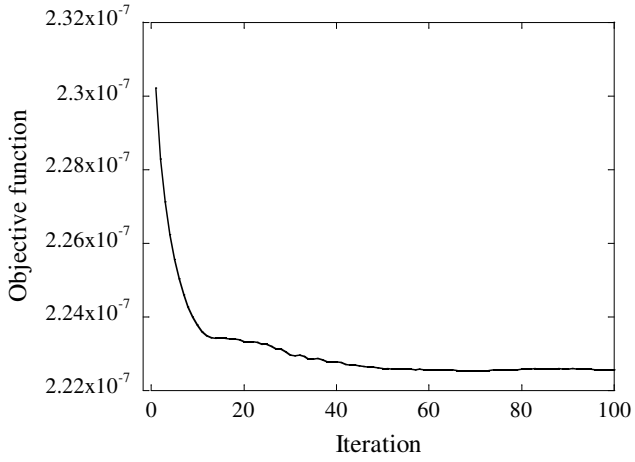

Figure 12: History of optimization for the first mode dominant vibration.

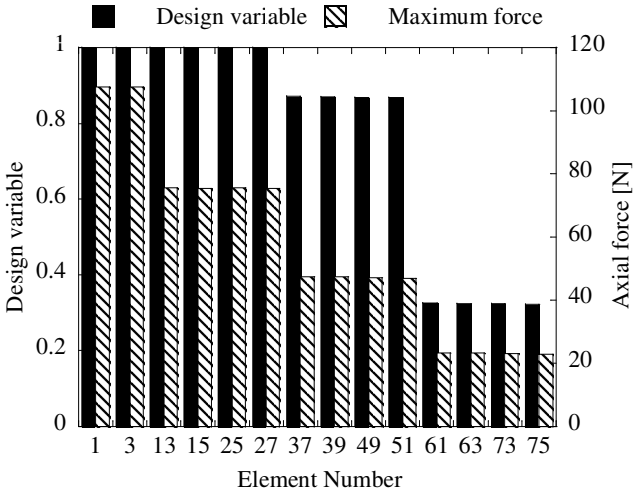

Figure 13: Comparison of the top 14 optimal design variables with the maximum force applied to these elements.

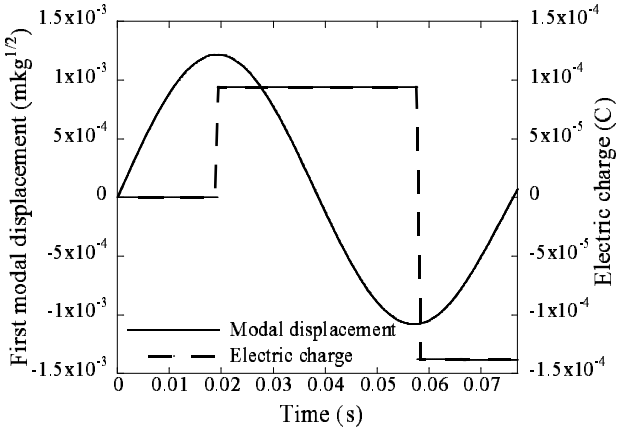

Figure 14: Variation of the first-order modal displacement and electric charging of the PZT.

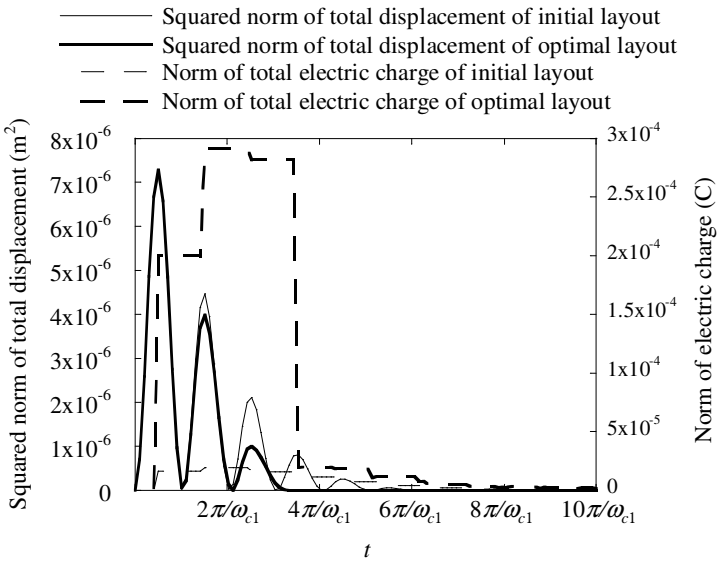

Figure 15: Time history of the squared norm of total displacement and norm of total electric charge of initial and optimal layout of PZT in re-analysis.

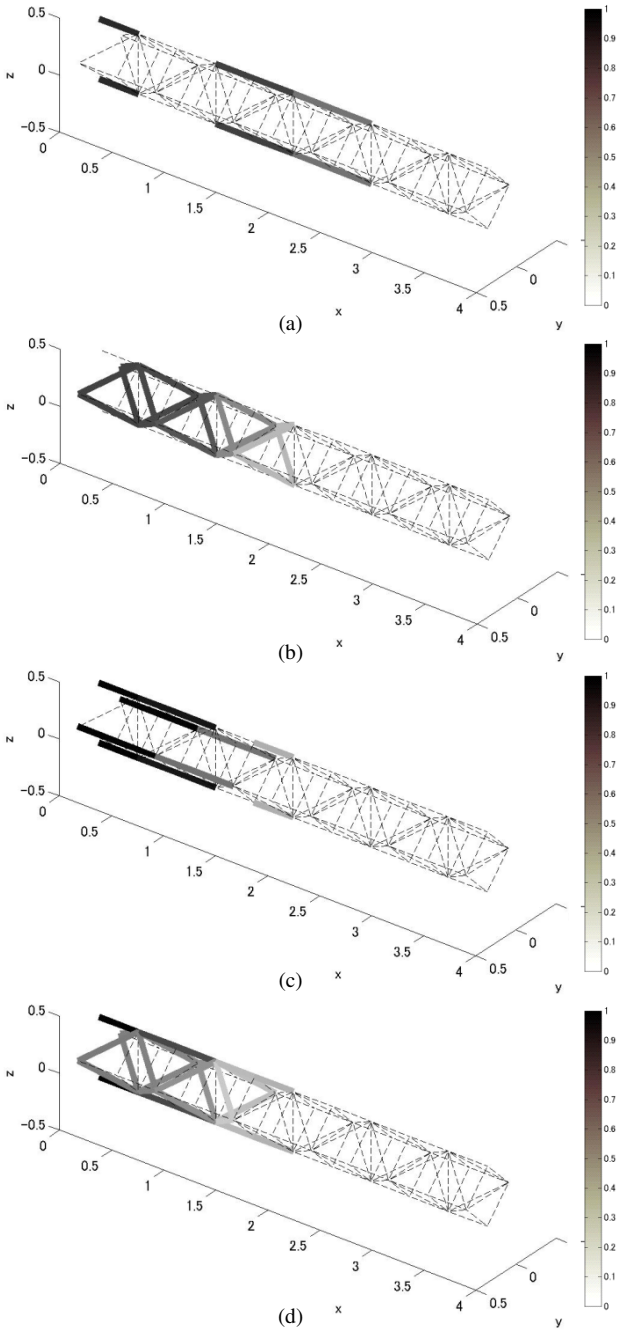

Figure 16: Optimal layout of PZTs for various vibration types. (a) through (d) correspond to Cases 2 through 5 described in the text.